Photothermal Imaging and Measurement of Protein Shell Stoichiometry of Single HIV-1 Gag Virus-like Nanoparticles

Mario Vieweger, Nancy Goicochea, Eun Sohl Koh, and Bogdan Dragnea*

Department of Chemistry, Indiana University, Bloomington, Indiana 47405, United States

Overstating the importance of viruses for life on Earth is difficult: associated with virtually every form of life, viruses are ubiquitous, obligated biological machineries lacking their own metabolism.[1] Viruses are drivers of major geochemical cycles, represent a force in the evolution of species, and stand for the largest reservoir of genetic material on Earth.[2,3] From a biotechnological point of view, viruses have evolved Nature's own targeted delivery nanovessels and could bring improved solubility, pharmacokinetics, biodistribution, and designed specificity when compared with small molecule drugs.[4]

Despite their fundamental part in the fabric of life and recent interest for nanotechnology, the underpinning details of the life stages of even the most studied viruses continued to remain obscure until relatively recently. With the first detection of a fluorescently labeled single virus in 1980,[5] a wealth of new insights started coming from studies of individual viruses during their interaction with the host.[6-8] For example, single virus tracking allowed an estimate of time scales for virus intracellular translocation,[9] mechanisms of transport prior cellular entry,[10] and heterogeneity of entry pathways.[11]

Through improved detectors,[12] probes,[13] and illumination schemes,[14] the impetus gained by single-molecule fluorescence microscopy has also fueled progress in real-time single-virus tracking.[7] With few notable exceptions,[15] *in singulo* studies of virus—host interactions have relied almost exclusively on fluorescence microscopy, and as a consequence, the scope of such observations remains at present limited by the intrinsic properties of fluorescent probes. In introducing the need for an alternative approach to real-time virus imaging, it is therefore worth examining how fluorescent probe limitations reflect on our capabilities of measuring dynamic processes at the scale of a single virus.

The small size of most viruses limits the number of fluorescent tags that can be applied to a virion before crowding effects start to interfere with virus function.[9] A high density of fluorescent labels may also lead to other adverse effects such as self-quenching.[16,17] We are thus led to the conclusion that, for single virus tracking, most of the time it is desirable to have only a few, sparsely distributed fluorophore tags. In these conditions, the total photon throughput is limited by photobleaching to 10^4-10^5 photons per fluorophore and therefore $\sim10^5-10^6$ photons per virus. At saturation excitation, this corresponds to an average time to photobleaching of a green fluorescent protein of ~4 ms for a maximum time resolution of ~20 ns.[18] The dynamic range

ABSTRACT Virus life stages often constitute a complex chain of events, difficult to track *in vivo* and in real-time. Challenges are associated with spatial and time limitations of current probes: most viruses are smaller than the diffraction limit of optical microscopes while the entire time scale of virus dynamics spans over 8 orders of magnitude. Thus, virus processes such as entry, disassembly, and egress have generally remained poorly understood. Here we discuss photothermal heterodyne imaging (PHI) as a possible alternative to fluorescence microscopy in the study of single virus-like nanoparticle (VNP) dynamics, with relevance in particular to virus uncoating. Being based on optical absorption rather than emission, PHI could potentially surpass some of the current limitations associated with fluorescent labels. As proof-of-principle, single VNPs self-assembled from 60 nm DNA-functionalized gold nanoparticles (DNA-Au NPs) encapsulated in a Gag protein shell of the human immunodeficiency virus (HIV-1) were imaged, and their photothermal response was compared with DNA-Au NPs. For the first time, the protein stoichiometry of a single virus-like particle was estimated by a method other than electron microscopy.

KEYWORDS: photothermal heterodyne imaging (PHI) · virus-like nanoparticles (VLPs) · HIV-1 Gag · protein shell stoichiometry

of fluorescence-based optical probes is therefore limited to 5–6 decades.

Virus dynamics associated with quaternary structure transformations and interactions with the host span approximately 8–10 decades, from microseconds estimated for the bending motions of the dihedral hinge between oligomeric structural subunits,[19] passing through milliseconds to minutes for fusion and cellular membrane translocation,[20] to several hours or even days corresponding to the systemic movement throughout an organism.[21]

Because of the several orders of magnitude difference in dynamic range between viruses and fluorescent probes, it would be challenging to follow by fluorescence rare but rapid processes. As a consequence, important phenomena such as virus self-assembly, disassembly, and genome delivery have remained until now beyond the reach of *in singulo* fluorescence-based methods. For such phenomena, a method providing an expanded dynamic range is required. The approach described here introduces such a method, which relies on the combination of two concepts: a virus mimetic probe composed of a virus protein shell (capsid) encapsulating a metal nanoparticle and an optical tracking method based upon the photothermal effect. It will be shown here that such a technique is able to rapidly locate and discriminate with quantitative accuracy between bare and virus-coated nanoparticles.

Previous structural and biochemical studies support the idea of *in vitro* self-assembled virus-like nanoparticles (VNPs) as biologically relevant mimics for viruses.[4,22–27] The hybrid biological/inorganic particle exhibits physical characteristics imparted by the nanoparticle core and shares some of the functional properties of the original virus capsid. For example, for certain core sizes, VNPs derived from brome mosaic virus (BMV) share the same icosahedral capsid motif and structural transitions with the wild-type virus.[28] Furthermore, successful cocrystallization at any ratio between native BMV virions and BMV-VLPs was reported which suggested that, even at molecular scale, the VNP surface is probably similar to the native virus surface.[23]

Due to the properties of the encapsulated core, a VNP is much easier to track than a virus. This may become particularly useful because, for example, following virus fate outside a host, in the environment, has been even more elusive than tracking single viruses inside cells. Versatility in incorporation of different types of nanoparticles such as quantum dots,[29] iron oxide,[30] and other magnetic particles as well as gold nanoparticles[22,31] illustrates well the potential held by VNPs for a wide range of imaging applications relying on fluorescence, magnetic resonance, scattering, or optical absorption.

Because of their higher spatial resolution than MRI, optical tracking methods based on fluorescence[32,33]

TABLE 1. Parameters Used for Numerical Solutions

layer	ρ (kg/m^3)	C_p (J/kgK)	κ (W/mK)	D (m^2/s)
AuNP	19300[a]	129[a]	317[a]	1.27×10^{-4b}
DNA	1688[c]	2025[e]	0.665[g]	1.94×10^{-7b}
protein (Gag)	1063[d]	1795[f]	0.2[h]	1.048×10^{-7b}
water	997[a]	4200[a]	0.616[a]	1.47×10^{-7b}

[a] COMSOL parameter databank. [b] Calculated according to $D = \kappa/\rho C_p$. [c] Calculated from molar weight of the ligands, # of ligands per Au NP estimated from Hurst *et al.*,[48] and volume in TEM and DLS experiments. [d] Calculated from molar weight of the proteins, average # of proteins.[49] [e] Sum of contributions from DNA[50] and tetraethylene glycol.[51] [f] Sum of contributions of the molar heat capacities of the comprising amino acids.[52] [g] Estimated from mass mixture of the ligands.[53–55] [h] Estimated from protein volume.[56]

and scattering[34,35] have been favored for imaging nanoparticle interactions with biological systems. Scattering-based imaging can overcome some of the challenges intrinsic to fluorescence imaging. However, the strong size dependence of the scattering cross section limits the applicability of light scattering microscopies to particles of >30 nm. This is a limitation especially important for small capsids, which cannot accommodate large payloads. Another challenge, particularly important for *in vivo* tracking, comes from the possible presence of other scattering centers, for example, cellular organelles.[34]

For small particles, it is more advantageous to use absorption as a contrast mechanism instead of scattering since the absorption effect scales as $\sim R^3$ (R = particle radius) instead of $\sim R^6$ for scattering.[36,37] Photothermal heterodyne imaging (PHI) belongs to the class of absorption-based techniques. Its contrast relies on the differences in absorption occurring between metal or semiconductor nanoparticles and a surrounding dielectric medium.[38–41] PHI detection limits reach down to 1.4 nm for gold particles, making it possible to record individual particle absorption spectra in essentially background-free conditions.[42,43] Furthermore, due to their large absorption cross sections, detection of metal nanoparticles by PHI was shown to be largely insensitive to the presence of much larger dielectric particles in solution,[38] allowing for robust tracking of Au NP-labeled biomolecules in turbid environments.[37] A feature of PHI that has recently been discussed is that signal strength depends on the surrounding medium such as the immersion liquid and thermal isolation of the substrate.[44] The largest contribution to this signal increase comes from the immediate surroundings of the nanoparticle; hence, finite changes in the nanoparticle characteristics, with dimensions close to the heat diffusion range, can increase the signal strength. For nanoparticles encapsulated in protein cages,[45] for example, the protein layer, which has a lower heat diffusion coefficient than water (see Table 1), will act as an insulating jacket for heat diffusion. The local temperature jump
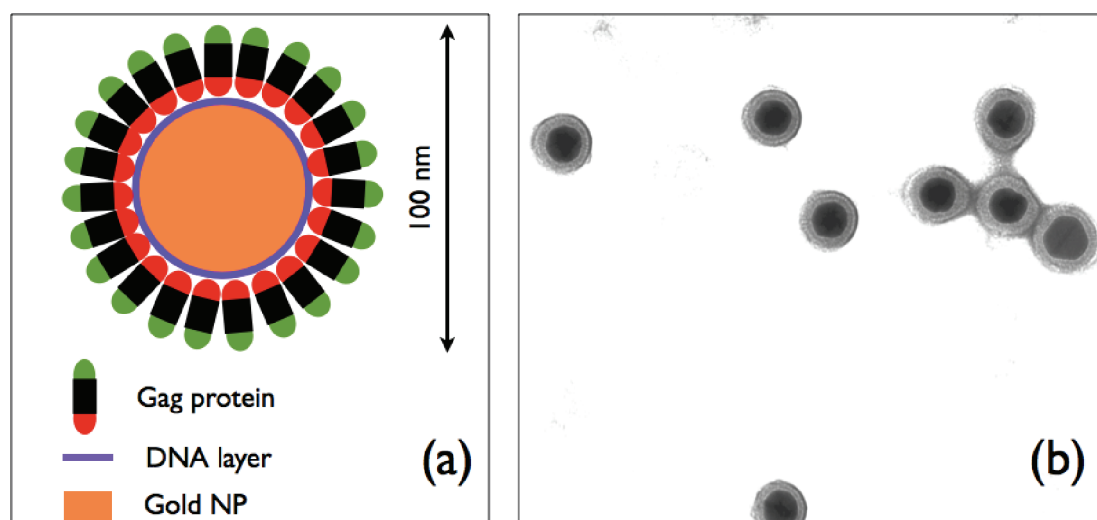
Figure 1. (a) Schematic of the Au−HIV Gag-VLP construct. (b) TEM picture of the assembly result. Average gold core diameter: 60 nm.

will be greater for a protein-coated particle than for an uncoated particle. Therefore, in principle, PHI could discriminate between protein-encapsulated nanoparticles and bare nanoparticles. This feature will give access to real-time optical measurements of the protein coverage *in vivo*, a potentially extremely useful application in the study of virus life stages and possibly of other protein-coated nanoparticles.[46] Pathways of processes like VNP disassembly and molecular recognition could be thus probed at the scale of a single particle and over virtually any length of time since there is no bleaching or blinking.

This paper represents a quantitative analysis of the effects that surrounding biomolecules have on PHI signal intensity. The first question to answer is whether the difference in signal between a naked core and a complete shell VLP is significant enough to warrant pursuing real-time experiments at laser intensities that leave the protein structure unaffected. This question will be addressed mainly theoretically in the first part of the paper. The second part will be concerned with an experimental application that validates the theoretical findings, namely, estimating protein shell stoichiometry for HIV-1 Gag-VNPs. To the best of our knowledge, this is the first time that a measurement of the average number of proteins constituting a virus shell was provided by an optical method.

RESULTS AND DISCUSSION

In PHI, illumination of noble metal nanoparticles with a resonant laser beam results in heating of the particle and subsequent thermal diffusion into the surrounding medium. The generated thermal diffusion profile causes a local change of the index of refraction with $\Delta n = (\partial n \partial T)\Delta T$, where $(\partial n \partial T) \approx 10^{-4}\,\mathrm{K}^{-1}$ for water at visible wavelengths.[47] The probe beam impinging on the transient inhomogeneous refractive index profile is

scattered by it, and interference of the scattered field E_{sc} with the unperturbed field E_{ref} generates the photothermal signal, $I_{PHI} \sim |E_{sc} + E_{ref}|^2$. Detection is facilitated by modulating the intensity of the pump laser beam and extracting the component of the signal at the modulation frequency Ω using a lock-in amplifier. Figure 2a provides a typical PHI map of a spread of DNA-coated 60 nm Au NPs.

Due to the small size of the Au NPs compared to the focal spot diameter, ω_0, of the heating laser, the absorbed laser power P_{abs} is given by the average power of the heating laser and the ratio of the cross sections of the particle absorption σ_{abs} and heating laser A. In the framework of a heat point source model for heat diffusion, the detected PHI signal can then be estimated from[44]

$$P_{abs} = \left(\frac{P_{heat}\sigma_{abs}}{A}\right)$$

$$S_{PHI} \approx \frac{\sigma_{abs}}{\pi\omega_0 A}n\frac{\partial n}{\partial T}\frac{P_{heat}P_{probe}\Delta t}{\lambda^2 C_p \Omega} \qquad (1)$$

where n is the temperature-dependent index of refraction, Ω is the modulation frequency, C_p is the specific heat capacity, Δt is the integration time of the lock-in amplifier, and P_{probe} and λ are the power and wavelength of the probe laser, respectively.

To explore in a simple way first the main idea of a particle coat-dependent signal, let us first assume that the protein layer is thick enough to be approximated by an infinite medium. For practical purposes, this would be a satisfactory approximation if the protein layer thickness was comparable with the width of the thermal diffusion profile corresponding to the modulation period. In this case, an analytical solution to the heat diffusion equation is available, which predicts a remarkable 2.5-fold increase in signal intensity for Au

NPs embedded in a protein medium compared to water. This significant increase is due to the difference
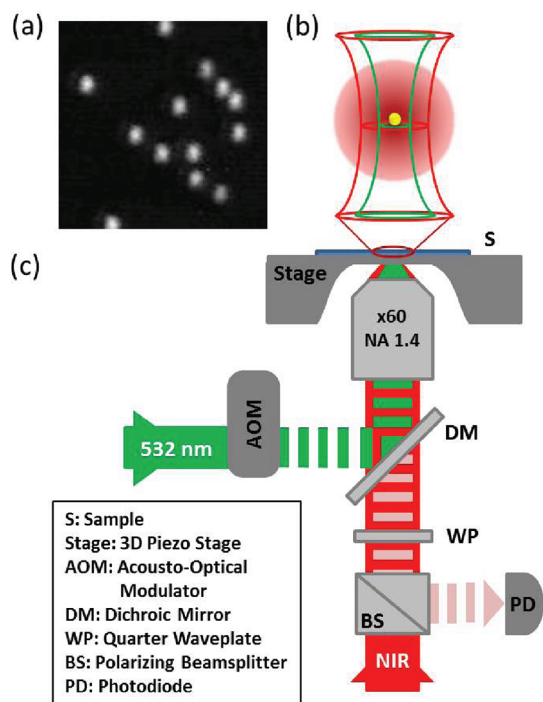
(a)

(b)

(c)

Stage

x60
NA 1.4

AOM

532 nm

DM

WP

S: Sample
Stage: 3D Piezo Stage
AOM: Acousto-Optical
Modulator
DM: Dichroic Mirror
WP: Quarter Waveplate
BS: Polarizing Beamsplitter
PD: Photodiode

BS

PD

NIR

S

Figure 2. Photothermal heterodyne imaging: (a) 5 × 5 μm PHI scan of 60 nm Au NPs taken at a heating intensity of 25 μW and probe intensity of 4 mW, (b) optical overlap in the focal point, (c) schematic of the optical setup.

in the heat capacities, C_p, of water and proteins of 4200 and 1795 J/kgK, respectively. However, a single protein layer covering the Au NPs is considerably thinner (5−15 nm) than the thermal diffusion length (∼1 μm). This approximate analytical model is therefore over-estimating the effects of a coating. In order to accurately determine if the signal increase from a thin protein layer is sufficient to distinguish between a VNP and a functionalized nanoparticle, a numerical model was utilized. Model parameters were based on an Au NP of 30 nm radius, with a surface-bound DNA 2.5 nm thick layer, covered by a 15 nm thick protein coat. These parameters have been chosen to match those measured by TEM on Au HIV-1 Gag-VNPs (Figure 1b). Heating by optical absorption and transient radial temperature profiles were simulated for Au NPs and Au-Gag-VNPs in water using the thermal parameters in Table 1.

Radial temperature distribution profiles corresponding to DNA-coated nanoparticle cores and VNPs at 2 μs after the beginning of the heating pulse are presented in Figure 3. The metal core exhibits uniform temperature over the entire volume ($R \leq 30$ nm, region A in Figure 3). At the gold−water interface, the temperature falls off rapidly and returns to 298 K within 2 μm from the center of the particle. As one can easily observe in Figure 3, a single additional molecular layer adsorbed onto the gold surface will significantly affect the thermal diffusion profile in the vicinity of the particle. Furthermore, thermal diffusion profiles show a steeper
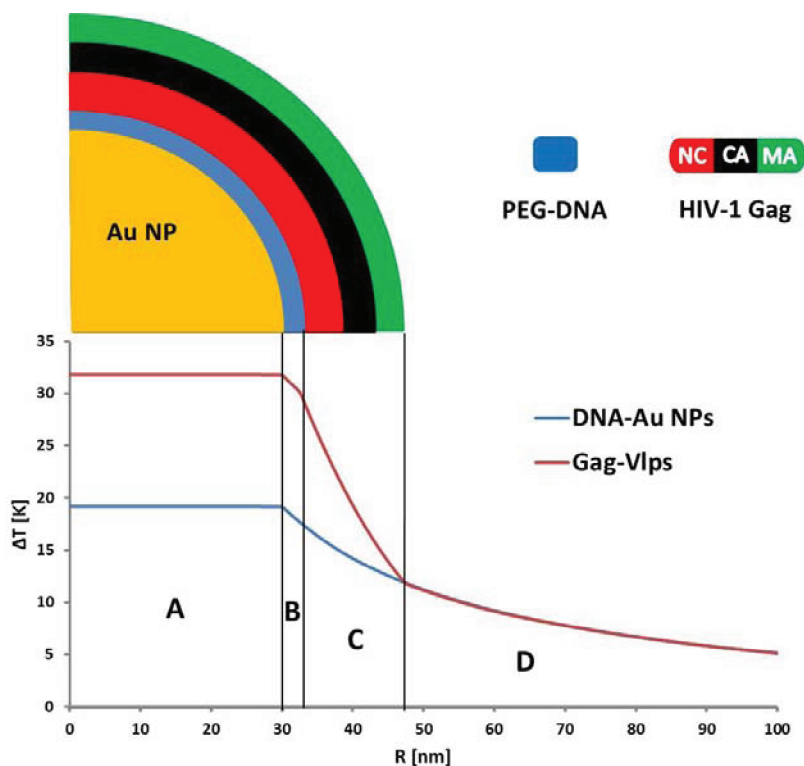
Au NP

PEG-DNA

HIV-1 Gag

NC CA MA

DNA-Au NPs

Gag-Vlps

Figure 3. Radial thermal diffusion profiles for DNA-coated Au NPs and Gag-VLPs at the center of the heating pulse. Heating laser intensity: 10 μW. (A) Within Au NP volume, (B) PEG-DNA layer, (C) HIV-1 Gag layer for VLPs, water for DNA-Au NPs, (D) water layer for both particles.
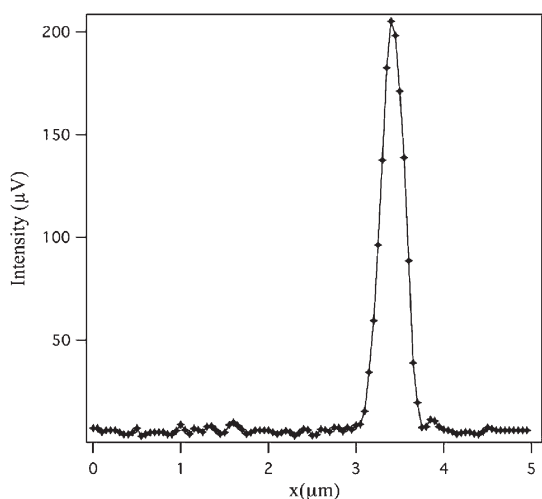
Figure 4. Raw PHI signal corresponding to a cross-sectional line profile passing through the center of a 60 nm DNA-coated Au NP in Figure 2a.

gradient within the protein layer at $30\ nm < R < 48\ nm$ (region C in Figure 3), while at $R > 48\ nm$ (region D in Figure 3), the Au-Gag-VLPs exhibit slightly lower temperatures than the DNA-Au NPs, especially toward the end of the heating pulse (Figure S1 in the Supporting Information). Since simulations were performed in conditions of the same amount of absorbed heat, the differences in the thermal diffusion profiles between DNA-Au NPs and Au-Gag-VLPs originate from the thermal properties of the materials and the thickness of their respective layers.

Due to the temperature dependence of the refractive index, this gives rise to a change in the optical signal that is proportional to the refractive index and thermo-optical coefficient of the medium surrounding the Au NP. In principle, two main effects contribute to the change of the optical signal in Au-Gag-VLPs, the change in the thermal diffusion profile (C_p) and a change in the optical response (n and dn/dT) of proteins compared to water. For Au-Gag-VLPs, the contribution from the change of n and dn/dT in the adsorbing layer was estimated at 2 and 4% of the total PHI signal, respectively (see Supporting Information). Hence, the temperature increase at the Au NP core is an adequate estimate of the signal change in PHI experiments on Au-Gag-VLPs. Note that the plot range in Figure 3 roughly corresponds to the radius of the diffraction-limited focal spot. Within this region, the differences in the thermal profiles of encapsulated and free NPs are significant: there is a temperature increase of ~60% predicted for a 15 nm thick protein layer. The next question is whether this change in temperature may lead to a detectable difference in the PHI signal.

In answering this question, let us consider a cross section through the raw experimental PHI signal coming from a 60 nm diameter Au particle at 25 μW heating power and 1 ms integration time per pixel (Figure 4).

The signal-to-noise ratio in this case was $S/N \approx 50$, while the signal-to-background ratio is $S/B \approx 34$. If based upon these numbers, we assume that the minimum detectable temperature difference corresponds to an $S/B \approx 2$, the minimum measurable ΔT within a bandwidth of 1 kHz is $\Delta T_{max}/17 = 1.2$ K. Therefore, thermal differences as large as those in Figure 3 should be well above the detection limit of the method. A direct consequence is that protein-coated and uncoated Au NPs should be distinguishable by PHI. Moreover, it should be actually possible to follow intermediate stages of uncoating by monitoring the protein surface coverage.

Surface coverage is important not only for determining the pathways of uncoating but also because virus capsids may, in general, be heterogeneous in their stoichiometry. This is believed to be the case for influenza and HIV, for example. With the exception of electron cryo-tomography, we are unaware of any other methods that can determine protein surface coverage at the scale of a single virus.

In particular, virus protein shells such as those of the immature HIV-1 Gag particle are believed to form incomplete cages,[57] while other viruses which have icosahedral symmetry have large pores organized in a symmetric array resembling wiffle balls.[25] The size of these pores depends on the virus type but can vary by as much as 20% as a function of environmental changes such as pH, for example, for certain plant viruses.[58−61] For these viruses, a change in the pore size will result in a change of the protein coverage and therefore thermal insulation efficiency. As a result, the transient temperature profile of the Au NPs will change depending on the state of the virus capsid. Therefore, the dependence of the degree of thermal insulation on the protein coverage could be used, in principle, to determine protein stoichiometry or structural rearrangement dynamics at the scale of a single particle.

To determine the magnitude of change that could be induced by protein coverage, the heat diffusion model geometry was adapted to incorporate cylindrical openings of variable size in the protein layer. Due to the radial dependence of heat diffusion away from the Au core, a simplified model was devised with openings equally distributed over the Au NP surface. The effect of varying the protein coverage was studied by changing the diameters of these openings and simulating the thermal diffusion for heating laser powers between 1 and 25 μW (see Supporting Information). Gradual decrease of the protein coverage results in a significant drop in temperature as soon as small openings in the protein layer appear. Thus, a 30% loss in protein coverage corresponds a greater than 50% drop in the peak temperature. Therefore, results of these numerical simulations suggest that PHI should be useful in determining the degree of completeness of a protein shell.

Besides protein adsorption or desorption, global molecular rearrangements in response to changes in the
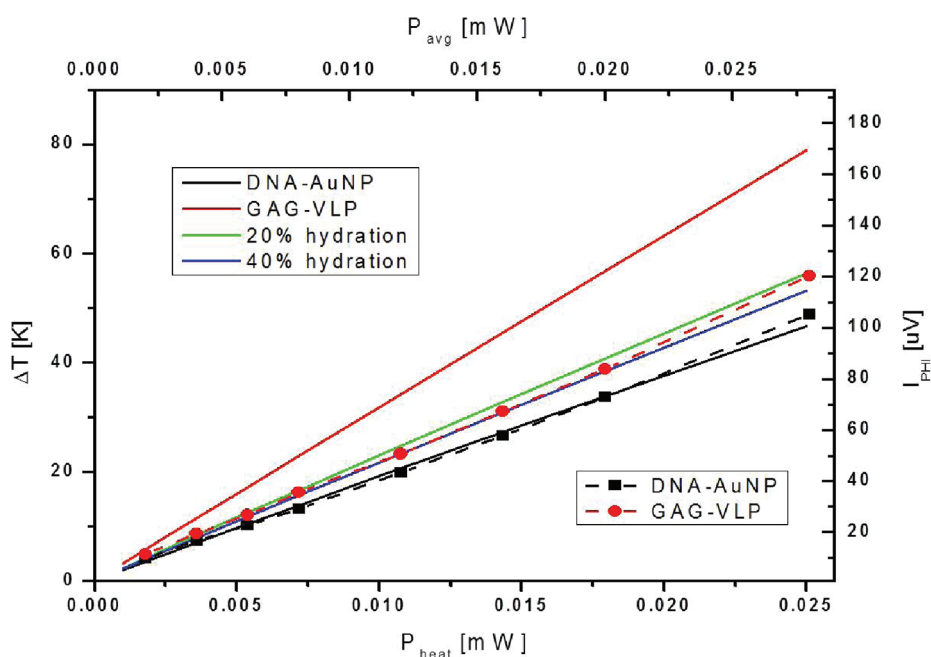
Figure 5. Experimental dependence of the PHI signal on the heating laser power for DNA-Au NPs and Gag-VLPs (right and top axis) and results from the theoretical model (left and bottom axis). In order to correlate theoretical and experimental findings, the scales were adjusted to overlap results for DNA-Au NPs (black curve and points).

environment can also lead to a change of the thermal properties of the protein capsid. For example, it is known that the protein heat capacity varies with the state of the protein, especially if structural rearrangements result in a change of the amount of protein surface that is exposed to the solvent.[62] Hence, the question of the importance of hydration for the thermal properties of the capsid proteins has to be considered since a change in the thermal properties of the protein layer will result in a change of the temperature profile around the particles. Studies by small-angle X-ray scattering and computational approaches reported a content of ~20–40% by weight of water for a wide range of proteins.[63] For globular proteins, for example, contributions from hydration account for between 15 and 40% of the total heat capacity corresponding to the native and unfolded states, respectively.[52] The hydration effect was studied here for volume ratios of water to proteins from 0 to 0.8 (Supporting Information, Figure S2).

In virus capsid transformations, a combination of both effects, surface coverage and protein hydration, may be expected in principle to occur which could render the PHI signal interpretation challenging. However, the results in Figures S1 and S2 suggest that the magnitude of the uncoating effect will exceed most of the time by far the one associated with reasonable hydration changes. However, knowledge of the thermal characteristics of the protein and the development of a specific model are necessary in order to fully benefit from the potential of PHI as a quantitative method.

Experiments to determine protein shell completeness by PHI were performed on the HIV-1 Gag-VLP system, which represents a model for the HIV-1 immature particle.[49] The HIV-1 Gag-VLPs were chosen to test the predictions from numerical simulations because they are believed to exhibit sizable gaps in their protein lattice.[49] The existence of gaps in the HIV-1 immature particles and HIV-1 Gag-VLPs was previously determined by electron tomography[57,64] but never by any other method. The current view on the native Gag shell is that of a lattice with openings shaped as scars resulting in a total surface coverage of ~70%.

PHI intensity data from 14 DNA-Au NPs and 21 Gag-VLPs were recorded for laser powers ranging from 2 to 28 μW. Average signal intensities were plotted against the average heating power (Figure 5). A linear regression of the data shows excellent fits with R^2 values better than 0.999 for both samples, indicating a good signal-to-noise ratio. The slope of the fits (dI_{PHI}/dP_{avg}) represents an instrument specific responsivity, an experimental figure-of-merit characterizing signal generation efficiency with respect to absorbed heat, integration time, probe laser power, and collection efficiency. Experiments are performed while keeping integration time (1 ms) and probe laser power (4 mW) constant to allow a comparison of signal intensities between DNA-Au NPs and Au-Gag-VLPs with results from numerical simulations.

Responsivities of 3.694 and 4.386 μV/μW were determined for DNA-Au NPs and Gag-VLPs, respectively. As predicted by simulations, the insulating effect of the Gag protein coat is lowering local thermal diffusivity
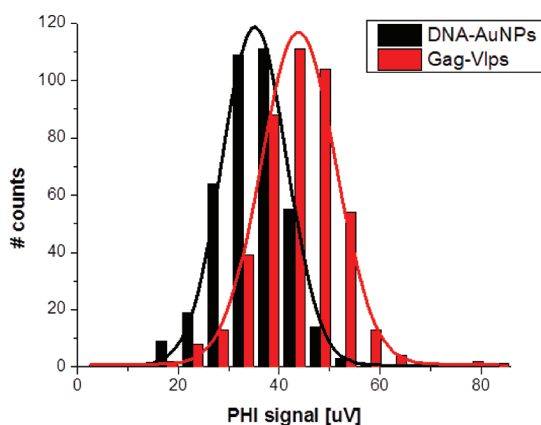
Figure 6. Distributions of signal intensities obtained from PHI experiments of DNA-Au NPs (black) and Gag-VLPs (red). The bars represent counts of signal intensities of individual particles in bin widths of 4 μV. The curves represent Gaussian fits with a mean and standard deviation of 34.9 and 6.87 μV for DNA-Au NPs and 43.55 and 8.31 μV for Gag-VLPs, respectively.

with the consequence of an average increase of 18.7% in PHI signal intensity. This signal increase lies well within the theoretically predicted range of 16.1−22.6% for protein hydrations of 40 and 20%, respectively, and a coverage of 70%, in agreement with the expectations from previous structural studies.

It is worth noting here that when PHI is to be applied to quantitative analysis *in singulo* careful consideration must be given to the core size polydispersity. The cubic power dependence of the signal on the particle radius results in a broader spread of intensity distribution.[65] For example, a sample of Au NPs with a size distribution of 10% will feature a spread of signal intensity of ∼30%. However, for time course experiments, this characteristic is not important. Figure 6 shows a comparison between the distributions of PHI signal intensities recorded from ensembles of DNA-Au NPs and Gag-VLPs in assembly buffer. That is, 386 individual DNA-Au NPs and 440 Gag-VLPs were imaged at a heating laser power of 10 μW and a probe laser power of 1.25 mW. These levels are 8 times lower than probe laser powers that have successfully been used for *in vivo* experiments.[66] The histograms display a monomodal size distribution, suggesting that dimers and other higher aggregates were absent from the measurements. The mean peak intensity for DNA-Au NPs was found to be 34.9 μV with a standard distribution of 6.87 μV (19.7%). Gag-VLPs were found to exhibit a mean intensity of 43.55 μV with a standard distribution of 8.31 μV (19.1%). This amounts to a 24.8% increase in PHI signal upon assembly of a HIV-1 Gag protein coat, while the standard distribution remained essentially the same. Comparison of the mean signal intensities (Table S1 in Supporting Infomration) obtained from histograms with the efficiencies determined from the heating intensity series of individual particles shows good overall agreement. The invariance of the

standard distribution after assembly suggests that broadening from coating is negligible with respect to the broadening due to core size polydispersity. The PHI signal increase of ∼25% corresponds to HIV-1 Gag-VLPs with an average surface coverage of 70% and a protein hydration of ∼15−20%.

A possible concern with PHI applications to protein systems is its reliance on a temperature jump, which could, in principle, denature the protein. The effect of the temperature increase in photothermal experiments on the surrounding biomolecules has been studied.[67] The midpoint for thermal denaturation T_m varies widely among proteins. The mean and median of 65 globular proteins, with known structure and thermodynamics of unfolding, were found to be 65.5 and 62.5 °C, respectively, ranging from 25 to 104 °C for individual proteins.[68] Assembly of individual proteins into hierarchical 3D structures such as protein cages enhances thermal stability, as observed for dimeric and assembled BMV proteins.[69]

For HIV-1, being a mammalian virus, physiological conditions occur at ∼310 K. Since PHI signals can be detected for temperature jumps of less than 5 K occurring for less than 1 μs, no structural distortion is expected for most proteins which are stable at room temperature.[70] Quantitative analysis may require larger temperature jumps. For example, according to Figure 5, a heating laser power of 10 μW results in a maximum temperature rise of ∼20 K at the particle surface. The temperature will fall to a value below 1% of the initial temperature in less than 2.5 μs. As all experiments are performed at room temperature, a maximum temperature of ∼45 °C was reached during PHI experiments. Hence the native temperature of the Gag proteins was never exceeded by more than 10 K, which is far below the average midpoint of denaturation for individual proteins.

Improvements in the S/N can be expected from thermal isolation of the substrate and an increase in the probe laser power,[44] hence, future applications have the potential of further lowering the temperature jump by a factor of 5 while maintaining the S/N.

As a final note, it is worth observing that, for a particle of the size of HIV-Gag-VLP (∼100 nm), ∼3000 copies of Gag protein are needed to assemble a capsid which covers 70% of the 60 nm particle core.[49] The ∼25% signal increase from the insulation due to the protein layer corresponds then to a contribution of ∼0.008% per protein and 0.05% per hexameric subunit. This is below the noise level of the current instrument, at least for temperatures that are reasonable for *in vivo* conditions. While 25% signal change is sufficient to determine whether the particle is assembled, individual assembly steps and subunit dynamics seem to be out of reach. However, for other viruses that require smaller Au core diameters, the number of proteins needed to form a complete capsid

will be considerably lower, and as a consequence, PHI will be potentially useful to evaluate individual steps of assembly.

CONCLUSION

In conclusion, we have demonstrated that changes in the local environment of Au NPs can be followed by photothermal heterodyne imaging. As a proof-of-principle, we have studied the change in the PHI signal due to the encapsulation of a nanoparticle by a virus protein coat. A numerical model was devised to study the theoretical effect of different physical and chemical factors on the strength and sensitivity of the PHI signal. In particular, the importance of the protein surface coverage and hydration was examined and illustrated through experiments done on HIV-1 Gag virus nanoparticles. A comparison of the temperature change observed in simulations shows good agreements with predicted relative signal strengths in PHI experiments.

For the first time, an optical method was used *in situ* as an alternative to TEM for estimating the protein surface coverage of an immature HIV-1 particle model. The results confirmed that 30% of the particle surface should be covered by gaps, a result found in agreement with previous knowledge from structural methods. The described methodology will open new ways of monitoring single nanoparticle—protein interactions.

METHODS

DNA-Au NP Functionalization. Gold nanoparticle solutions were purchased from British Biocell International. TEM analysis of 500 particles resulted in an average diameter of 56 nm (relative standard deviation: 10%). Functionalization with 5′-thiol-modified PEG-DNA oligonucleotides (5′-HS-3[(CH$_2$CH$_2$O)$_6$ phosphoramidite]-(TG)$_{25}$-3′) was carried out with slight modifications of the Hurst *et al.* protocol.[48] Briefly, freshly reduced disulfide bonds at the 5′-end of the nucleotides were added to the gold nanoparticles at a ratio of 3 equiv of DNA/1 equiv of Au. Typical gold and DNA amounts were 10 mL (from stock bottle) and 2 mg, respectively. After 2 h incubation, the mixture was brought to 0.01 M in phosphate buffer (PB, pH 8) and 0.01% in sodium dodecyl sulfate (SDS). After another 90 min incubation, the mixture was brought to 0.05 M NaCl in PBS and then 0.1 M followed by sonication for 10 s. The ionic strength was subsequently increased to 1 at 0.1 M intervals and spaced every 15 min. Thereafter, the reaction was incubated for 2 days at room temperature in order to ensure oligonucleotide saturation of the nanoparticle surface. The excess oligonucleotide was removed through centrifugation (38 000*g*, 40 min, 4 °C, Beckman, floor model preparative ultracentrifuge, type 50.2Ti rotor). Precipitated DNA-PEG-Au conjugates were resuspended in high ionic strength buffer (50 mM HEPES, 0.5 M NaCl, pH 7.5) and washed for a total of five times. The final pellet was resuspended and stored in water. This procedure achieves an average coverage of ~2000 fifty-base ssDNAs per Au NP.[49]

Gag-VLP Assembly. The major structural element of the HIV-1 immature particle, the Gag polyprotein, contains four major domains: the matrix (MA), capsid (CA), nucleocapsid (NC), and the C-terminal p6.[71] The first three domains are required for virus particle assembly. The minimal set of required components for *in vitro* assembly of Gag-VLPs into virus-like particles are the HIV Gag polyprotein or assembly competent recombinant versions of Gag, such as the recombinant Δ16-99 Gag[72,73] and a source of nucleic acid. Encapsulation of Au NPs by recombinant Δ16-99 Gag was carried out by adapting the Datta *et al.* protocol (Figure 1).[74] The deleted Gag protein construct lacks the myristylated acid for improved solubility. In addition, the p6 domain at the C-terminal region was missing since it does not play a role for *in vitro* assembly.[72,75]

Typically, *in vitro* assembly of Δ16-99 Gag around gold cores was induced at a number ratio of 15 000 equiv of Gag to 1 equiv of gold. The concentration of gold particles was calculated from its absorbance value at 450 nm, taking into account the relationship between the molar extinction coefficient and the particle size.[76] Prior to mixing with Δ16-99 Gag, DNA-PEG-Au in water was buffer exchanged with high ionic strength buffer (50 mM HEPES, 0.5 M NaCl, pH 7.5) at room temperature and mixed with the corresponding amount of concentrated recombinant Gag in storage buffer (50 mM HEPES, 0.5 M NaCl, 4 mM DTT, pH 7.5).

The mixture was diluted with high ionic strength buffer to a final protein concentration of 1 mg/mL. The assembly reaction was dialyzed (20k MWCO) overnight against low ionic strength buffer (50 mM HEPES, 0.1 M NaCl, 1 mM DTT, pH 8.0) at 4 °C. Next day, assembly products in the form of HIV-1 Gag VNPs were recovered from the dialysis bag and concentrated (300k MWCO, 7000*g*, 4 °C) for EM analysis or subjected to a second dialysis (100k MWCO) for removal of unbound Gag.

Sample Preparation for Imaging. Sample chambers for microscopy were assembled from two coverslips (VWR micro cover glass, 24 × 60 mm, No. 1^1/$_2$) separated by double-sided adhesive tape with a thickness of ~70 μm. The coverslips were cleaned with piranha solution and coated with poly(lysine) (Sigma-Aldrich, poly-L-lysine solution, P8920) to ensure immobilization of particles on the surface. The double-sided tape had a narrow channel cut out that acted as sample reservoir (typical dimensions: 1 mm × 70 μm × 3 cm). After the sample chamber was assembled, ~2 μL of sample was added and incubated for 30 min before the cell was mounted onto the microscope. Samples for PHI were prepared in assembly buffer (50 mM HEPES, 0.1 M NaCl, 1 mM DTT, pH 8.0) with a concentration of 3 × 10^{10} particles/mL.

Photothermal Heterodyne Imaging (PHI). The PHI setup (Figure 2) is based upon a stage-scanning confocal microscope with two collinear laser beams focused to the same point inside the sample.[65] It consists of an amplitude-modulated pump laser (Compass 315M, Coherent, Inc.) tuned to the plasmon frequency of the Au NPs at ~532 nm and a nonresonant probe laser at 785 nm (LPM785-80C, Newport, Inc.). Amplitude modulation of the pump laser with a carrier frequency of 250 kHz is achieved by an acousto-optical modulator (35250-.2-.53-XQ, Neos Technologies). Overlap of the two lasers in the focal spot (Figure 2b) is achieved by a high NA objective (Nikon CFI Plan Apo VC 60× oil, NA 1.40) that is also used to collimate backscattered light from the sample. The energy absorbed by the Au NP is released as heat into the medium. The transient temperature jump induces a local change of the index of refraction of the medium around the nanoparticle. The probe light scattered by the transient refraction index perturbation is detected by taking advantage of the phase shift in circularly polarized light using a fiber-coupled PIN photodiode. Photodiode signal at the modulation frequency was fed into a 2 MHz bandwidth lock-in amplifier (Model 7280, Signal Recovery). Confocal scanning and analysis of the recorded data are performed *via* a software algorithm written in Labview (Labview 2009, National Instruments).

Numeric Simulations. Simulations were performed by numerically solving the three-dimensional heat equation by the finite element method (Heat Transfer Module, Comsol Multiphysics 3.5a, Comsol, Inc.). Model geometries were created by placing the NP of interest in the center of a 5 μm water reservoir. Predefined mesh sizes were used, and boundary layers were added, if necessary, to ensure heat was not accrued at the

interfaces due to mesh size mismatches. The problem was treated as time-dependent and solved using the conjugate gradient linear system solver with the algebraic multigrid preconditioner. Time stepping was done according the BDF method, and steps were calculated every 100 ns over the entire range of a 4 μs heating pulse.

Supporting Information Available: Effects of the thermal (Figure S1) and optical properties of the protein coat on the optical signal, effects of changes in the refractive index on the width and intensity of the absorption cross section at the plasmon frequency (Figure S3), effects of surface coverage (Figure S3) and protein hydration (Figure S4) on thermal diffusion and comparison of experimental results from distributions with heating laser power series (Table S1). This material is available free of charge *via* the Internet at http://pubs.acs.org.

REFERENCES AND NOTES

1. Smart, A. C.; Harper, D. M. Life after Lakes: The Ecology and Management of the Water Distribution Network. *Hydrobiologia* **1999**, *395/396*, 379–386.
2. Suttle, C. A. Viruses in the Sea. *Nature* **2005**, *437*, 356–361.
3. Hamilton, G. Virology: The Gene Weavers. *Nature* **2006**, *441*, 683–685.
4. Manchester, M.; Steinmetz, N. F. Viruses and Nanotechnology. Preface. *Curr. Top. Microbiol. Immunol.* **2009**, *327*, v–vi.
5. Helenius, A.; Kartenbeck, J.; Simons, K.; Fries, E. On the Entry of Semliki Forest Virus into Bhk-21 Cells. *J. Cell Biol.* **1980**, *84*, 404–420.
6. Burckhardt, C. J.; Greber, U. F. Redox Rescues Virus from Er Trap. *Nat. Cell Biol.* **2008**, *10*, 9–11.
7. Kukura, P.; Ewers, H.; Mueller, C.; Renn, A.; Helenius, A.; Sandoghdar, V. High-Speed Nanoscopic Tracking of the Position and Orientation of a Single Virus. *Nat. Methods* **2009**, *6*, 923–927.
8. Brandenburg, B.; Zhuang, X. Virus Trafficking—Learning from Single-Virus Tracking. *Nat. Rev. Microbiol.* **2007**, *5*, 197–208.
9. Seisenberger, G.; Ried, M. U.; Endress, T.; Buening, H.; Hallek, M.; Brauchle, C. Real-Time Single-Molecule Imaging of the Infection Pathway of an Adeno-Associated Virus. *Science* **2001**, *294*, 1929–1932.
10. Lehmann, M. J.; Sherer, N. M.; Marks, C. B.; Pypaert, M.; Mothes, W. Actin- and Myosin-Driven Movement of Viruses along Filopodia Precedes Their Entry into Cells. *J. Cell Biol.* **2005**, *170*, 317–325.
11. Rust, M. J.; Lakadamyali, M.; Zhang, F.; Zhuang, X. Assembly of Endocytic Machinery around Individual Influenza Viruses during Viral Entry. *Nat. Struct. Mol. Biol.* **2004**, *11*, 567–573.
12. Michalet, X.; Siegmund, O. H. W.; Vallerga, J. V.; Jelinsky, P.; Millaud, J. E.; Weiss, S. Detectors for Single-Molecule Fluorescence Imaging and Spectroscopy. *J. Mod. Opt.* **2007**, *54*, 239–281.
13. Shaner, N. C.; Steinbach, P. A.; Tsien, R. Y. A Guide to Choosing Fluorescent Proteins. *Nat. Methods* **2005**, *2*, 905–909.
14. Patterson, G.; Davidson, M.; Manley, S.; Lippincott-Schwartz, J. Superresolution Imaging Using Single-Molecule Localization. *Annu. Rev. Phys. Chem.* **2010**, *61*, 345–368.
15. Gladnikoff, M.; Rousso, I. Directly Monitoring Individual Retrovirus Budding Events Using Atomic Force Microscopy. *Biophys. J.* **2008**, *94*, 320–326.
16. Brandenburg, B.; Lee, L. Y.; Lakadamyali, M.; Rust, M. J.; Zhuang, X.; Hogle, J. M. Imaging Poliovirus Entry in Live Cells. *PLoS Biol.* **2007**, *5*, 1543–1555.
17. Geddes, C. D.; Lakowicz, J. R., Eds. *Reviews in Fluorescence 2006*; Springer: New York, **2006**; Vol. *3*, 604 pp.
18. Harms, G. S.; Cognet, L.; Lommerse, P. H. M.; Blab, G. A.; Schmidt, T. Autofluorescent Proteins in Single-Molecule Research: Applications to Live Cell Imaging Microscopy. *Biophys. J.* **2001**, *80*, 2396–2408.
19. van Vlijmen, H. W. T.; Karplus, M. Normal Mode Calculations of Icosahedral Viruses with Full Dihedral Flexibility by Use of Molecular Symmetry. *J. Mol. Biol.* **2005**, *350*, 528–542.
20. Marsh, M.; Helenius, A. Virus Entry: Open Sesame. *Cell* **2006**, *124*, 729–740.
21. Fisher, K. Striking out at Disseminated Metastases: The Systemic Delivery of Oncolytic Viruses. *Curr. Opin. Mol. Ther.* **2006**, *8*, 301–313.
22. Chen, C.; Daniel, M.-C.; Quinkert, Z. T.; De, M.; Stein, B.; Bowman, V. D.; Chipman, P. R.; Rotello, V. M.; Kao, C. C.; Dragnea, B. Nanoparticle-Templated Assembly of Viral Protein Cages. *Nano Lett.* **2006**, *6*, 611–615.
23. Sun, J.; DuFort, C.; Daniel, M.-C.; Murali, A.; Chen, C.; Gopinath, K.; Stein, B.; De, M.; Rotello, V. M.; Holzenburg, A.; *et al.* Core-Controlled Polymorphism in Virus-like Particles. *Proc. Natl. Acad. Sci. U.S.A.* **2007**, *104*, 1354–1359.
24. Daniel, M.-C.; Tsvetkova, I. B.; Quinkert, Z. T.; Murali, A.; De, M.; Rotello, V. M.; Kao, C. C.; Dragnea, B. Role of Surface Charge Density in Nanoparticle-Templated Assembly of Bromovirus Protein Cages. *ACS Nano* **2010**, *4*, 3853–3860.
25. Kang, S.; Uchida, M.; O'Neil, A.; Li, R.; Prevelige, P. E.; Douglas, T. Implementation of P22 Viral Capsids as Nanoplatforms. *Biomacromolecules* **2010**, *11*, 2804–2809.
26. Lockney, D. M.; Guenther, R. N.; Loo, L.; Overton, W.; Antonelli, R.; Clark, J.; Hu, M.; Luft, C.; Lommel, S. A.; Franzen, S. The Red Clover Necrotic Mosaic Virus Capsid as a Multifunctional Cell Targeting Plant Viral Nanoparticle. *Bioconjugate Chem.* **2011**, *22*, 67–73.
27. Loo, L.; Guenther, R. H.; Lommel, S. A.; Franzen, S. Encapsidation of Nanoparticles by Red Clover Necrotic Mosaic Virus. *J. Am. Chem. Soc.* **2007**, *129*, 11111–11117.
28. Chen, C.; Daniel, M. C.; Quinkert, Z. T.; De, M.; Stein, B.; Bowman, V. D.; Chipman, P. R.; Rotello, V. M.; Kao, C. C.; Dragnea, B. Nanoparticle-Templated Assembly of Viral Protein Cages. *Nano Lett.* **2006**, *6*, 611–615.
29. Dixit, S. K.; Goicochea, N. L.; Daniel, M.-C.; Murali, A.; Bronstein, L.; De, M.; Stein, B.; Rotello, V. M.; Kao, C. C.; Dragnea, B. Quantum Dot Encapsulation in Viral Capsids. *Nano Lett.* **2006**, *6*, 1993–1999.
30. Huang, X.; Bronstein, L. M.; Retrum, J.; Dufort, C.; Tsvetkova, I.; Aniagyei, S.; Stein, B.; Stucky, G.; McKenna, B.; Remmes, N.; *et al.* Self-Assembled Virus-like Particles with Magnetic Cores. *Nano Lett.* **2007**, *7*, 2407–2416.
31. Dragnea, B.; Chen, C.; Kwak, E.-S.; Stein, B.; Kao, C. C. Gold Nanoparticles as Spectroscopic Enhancers for *In Vitro* Studies on Single Viruses. *J. Am. Chem. Soc.* **2003**, *125*, 6374–6375.
32. Gao, X.; Wang, T.; Wu, B.; Chen, J.; Chen, J.; Yue, Y.; Dai, N.; Chen, H.; Jiang, X. Quantum Dots for Tracking Cellular Transport of Lectin-Functionalized Nanoparticles. *Biochem. Biophys. Res. Commun.* **2008**, *377*, 35–40.
33. Montiel, D.; Yang, H. Real-Time Three-Dimensional Single-Particle Tracking Spectroscopy for Complex Systems. *Laser Photonics Rev.* **2010**, *4*, 374–385.
34. Qian, W.; Huang, X.; Kang, B.; El-Sayed, M. A. Dark-Field Light Scattering Imaging of Living Cancer Cell Component from Birth through Division Using Bioconjugated Gold Nanoprobes. *J. Biomed. Opt.* **2010**, *15*, 046025/1–046025/9.
35. Nan, X.; Sims, P. A.; Xie, X. S. Organelle Tracking in a Living Cell with Microsecond Time Resolution and Nanometer Spatial Precision. *ChemPhysChem* **2008**, *9*, 707–712.
36. van Dijk, M. A.; Lippitz, M.; Orrit, M. Far-Field Optical Microscopy of Single Metal Nanoparticles. *Acc. Chem. Res.* **2005**, *38*, 594–601.
37. Van Dijk, M. A.; Tchebotareva, A. L.; Orrit, M.; Lippitz, M.; Berciaud, S.; Lasne, D.; Cognet, L.; Lounis, B. Absorption and Scattering Microscopy of Single Metal Nanoparticles. *Phys. Chem. Chem. Phys.* **2006**, *8*, 3486–3495.

38. Boyer, D.; Tamarat, P.; Maali, A.; Lounis, B.; Orrit, M. Photothermal Imaging of Nanometer-Sized Metal Particles among Scatterers. *Science* **2002**, *297*, 1160–1163.

39. Cognet, L.; Berciaud, S.; Lasne, D.; Lounis, B. Photothermal Methods for Single Nonluminescent Nano-Objects. *Anal. Chem.* **2008**, *80*, 2288–2294.

40. Cognet, L.; Tardin, C.; Boyer, D.; Choquet, D.; Tamarat, P.; Lounis, B. Single Metallic Nanoparticle Imaging for Protein Detection in Cells. *Proc. Natl. Acad. Sci. U.S.A.* **2003**, *100*, 11350–11355.

41. Giblin, J.; Syed, M.; Banning, M. T.; Kuno, M.; Hartland, G. Experimental Determination of Single Cdse Nanowire Absorption Cross Sections through Photothermal Imaging. *ACS Nano* **2010**, *4*, 358–364.

42. Berciaud, S.; Cognet, L.; Lounis, B. Photothermal Absorption Spectroscopy of Individual Semiconductor Nanocrystals. *Nano Lett.* **2005**, *5*, 2160–2163.

43. Carey, C. R.; Le Bel, T.; Crisostomo, D.; Giblin, J.; Kuno, M.; Hartland, G. V. Imaging and Absolute Extinction Cross-Section Measurements of Nanorods and Nanowires through Polarization Modulation Microscopy. *J. Phys. Chem. C* **2010**, *114*, 16029–16036.

44. Gaiduk, A.; Ruijgrok, P. V.; Yorulmaz, M.; Orrit, M. Detection Limits in Photothermal Microscopy. *Chem. Sci.* **2010**, *1*, 343–350.

45. Moyano, D. F.; Rotello, V. M. Nano Meets Biology: Structure and Function at the Nanoparticle Interface. *Langmuir* **2011**, 10.1021/la2004535.

46. Rana, S.; Yeh, Y. C.; Rotello, V. M. Engineering the Nanoparticle−Protein Interface: Applications and Possibilities. *Curr. Opin. Chem. Biol.* **2010**, *14*, 828–834.

47. Dorsey, N. E. *Properties of Ordinary Water-Substance*; Reinhold Publishing Corp.: New York, 1940.

48. Hurst, S. J.; Lytton-Jean, A. K. R.; Mirkin, C. A. Maximizing DNA Loading on a Range of Gold Nanoparticle Sizes. *Anal. Chem.* **2006**, *78*, 8313–8318.

49. Goicochea, N. L.; Datta, S. A. K.; Ayaluru, M.; Kao, C.; Rein, A.; Dragnea, B. Structural Properties of Template-Directed Recombinant Hiv-1 Gag Particles. *J. Mol. Biol.* **2011**in press.

50. Mrevlishvili, G. M. Low-Temperature Heat Capacity of Biomacromolecules and the Entropic Cost of Bound Water in Proteins and Nucleic Acids (DNA). *Thermochim. Acta* **1998**, *308*, 49–54.

51. Wen, J. Heat Capacities of Polymers. *Phys. Prop. Polym. Handb.* **1996**, 101–109.

52. Gomez, J.; Hilser, V. J.; Xie, D.; Freire, E. The Heat Capacity of Proteins. *Proteins Struct., Funct., Genet.* **1995**, *22*, 404–412.

53. Tuliszka, M.; Jaroszyk, F. Thermal Conductivity Measurements of tRNA Melting Process. *Thermochim. Acta* **1993**, *219*, 355–360.

54. Khayet, M.; Ortiz de Zarate, J. M. Application of the Multi-Current Transient Hot-Wire Technique for Absolute Measurements of the Thermal Conductivity of Glycols. *Int. J. Thermophys.* **2005**, *26*, 637–646.

55. Tuliszka, M.; Jaroszyk, F. A New Method of Investigation of the DNA Melting Process. The Thermal Conductivity Method. *Thermochim. Acta* **1992**, *194*, 67–75.

56. Lervik, A.; Bresme, F.; Kjelstrup, S.; Bedeaux, D.; Miguel Rubi, J. Heat Transfer in Protein−Water Interfaces. *Phys. Chem. Chem. Phys.* **2010**, *12*, 1610–1617.

57. Briggs, J. A. G.; Riches, J. D.; Glass, B.; Bartonova, V.; Zanetti, G.; Kraeusslich, H. G., Structure and Assembly of Immature Hiv. *Proc. Natl. Acad. Sci. U.S.A.* **2009**, *106*, 11090−11095, S11090/1−S11090/9.

58. Zulauf, M. Swelling of Brome Mosaic Virus as Studied by Intensity Fluctuation Spectroscopy. *J. Mol. Biol.* **1977**, *114*, 259–266.

59. Bancroft, J. B.; Hills, G. J.; Markham, R. The Self-Assembly Process in a Small Spherical Virus. Formation of Organized Structures from Protein Subunits *in Vitro*. *Virology* **1967**, *31*, 354–379.

60. Speir, J. A.; Munshi, S.; Wang, G.; Baker, T. S.; Johnson, J. E. Structures of the Native and Swollen Forms of Cowpea Chlorotic Mottle Virus Determined by X-ray Crystallography and Cryo-electron Microscopy. *Structure* **1995**, *3*, 63–78.

61. Douglas, T.; Young, M. Host−Guest Encapsulation of Materials by Assembled Virus Protein Cages. *Nature* **1998**, *393*, 152–155.

62. Yang, P.-H.; Rupley, J. A. Protein−Water Interactions. Heat Capacity of the Lysozyme−Water System. *Biochemistry* **1979**, *18*, 2654–2661.

63. Durchschlag, H.; Zipper, P. Volume, Surface and Hydration Properties of Proteins. *Prog. Colloid Polym. Sci.* **2008**, *134*, 19–29.

64. Wright, E. R.; Schooler, J. B.; Ding, H. J.; Kieffer, C.; Fillmore, C.; Sundquist, W. I.; Jensen, G. J. Electron Cryotomography of Immature HIV-1 Virions Reveals the Structure of the Ca and Sp1 Gag Shells. *EMBO J.* **2007**, *26*, 2218–2226.

65. Berciaud, S.; Lasne, D.; Blab, G. A.; Cognet, L.; Lounis, B. Photothermal Heterodyne Imaging of Individual Metallic Nanoparticles: Theory *versus* Experiment. *Phys. Rev. B: Condens. Matter Mater. Phys.* **2006**, *73*, 045424/1–045424/8.

66. Leduc, C.; Jung, J.-M.; Carney, R. R.; Stellacci, F.; Lounis, B. Direct Investigation of Intracellular Presence of Gold Nanoparticles *via* Photothermal Heterodyne Imaging. *ACS Nano* **2011**, *5*, 2587–2592.

67. Pustovalov, V. K.; Smetannikov, A. S.; Zharov, V. P. Photothermal and Accompanied Phenomena of Selective Nano-photothermolysis with Gold Nanoparticles and Laser Pulses. *Laser Phys. Lett.* **2008**, *5*, 775–792.

68. Robertson, A. D.; Murphy, K. P. Protein Structure and the Energetics of Protein Stability. *Chem. Rev.* **1997**, *97*, 1251–1267.

69. Hema, M.; Murali, A.; Ni, P.; Vaughan, R. C.; Fujisaki, K.; Tsvetkova, I.; Dragnea, B.; Kao, C. C. Effects of Amino Acid Substitutions in the Brome Mosaic Virus Capsid Protein on RNA Encapsidation. *Mol. Plant-Microbe Interact.* **2010**, *23*, 1433–1447.

70. Sochava, I. V.; Smirnova, O. I.; Barynin, V. V.; Belopol'skaya, T. V.; Kazitsyna, S. Y. Time-Related Thermal Stability of Proteins in Concentrated Solutions. *Mol. Biol.* **1982**, *16*, 386–391.

71. Ganser-Pornillos, B. K.; Yeager, M.; Sundquist, W. I. The Structural Biology of HIV Assembly. *Curr. Opin. Struct. Biol.* **2008**, *18*, 203–217.

72. Campbell, S.; Fisher, R. J.; Towler, E. M.; Fox, S.; Issaq, H. J.; Wolfe, T.; Phillips, L. R.; Rein, A. Modulation of HIV-like Particle Assembly *in Vitro* by Inositol Phosphates. *Proc. Natl. Acad. Sci. U.S.A.* **2001**, *98*, 10875–10879.

73. Gross, I.; Hohenberg, H.; Wilk, T.; Wiegers, K.; Grattinger, M.; Muller, B.; Fuller, S.; Krausslich, H.-G. A Conformational Switch Controlling HIV-1 Morphogenesis. *EMBO J.* **2000**, *19*, 103–113.

74. Datta, S. A. K.; Rein, A. Preparation of Recombinant HIV-1 Gag Protein and Assembly of Virus-like Particles *in Vitro*. *Methods Mol. Biol.* **2009**, *485*, 197–208.

75. Campbell, S.; Rein, A. *In Vitro* Assembly Properties of Human Immunodeficiency Virus Type 1 Gag Protein Lacking the P6 Domain. *J. Virol.* **1999**, *73*, 2270–2279.

76. Haiss, W.; Thanh, N. T. K.; Aveyard, J.; Fernig, D. G. Determination of Size and Concentration of Gold Nanoparticles from UV−Vis Spectra. *Anal. Chem.* **2007**, *79*, 4215–4221.